PHYSICS OF FLUIDS **27**, 073302 (2015)

Coalescence and breakup of large droplets in turbulent channel flow

Luca Scarbolo,[a] Federico Bianco,[b] and Alfredo Soldati[c]
Department of Electrical, Management and Mechanical Engineering, University of Udine, Udine 33100, Italy

(Received 13 January 2015; accepted 18 June 2015; published online 7 July 2015)

Coalescence and breakup of large deformable droplets dispersed in a wall-bounded turbulent flow are investigated. Droplets much larger than the Kolmogorov length scale and characterized by a broad range of surface tension values are considered. The turbulent field is a channel flow computed with pseudo-spectral direct numerical simulations, while phase interactions are described with a phase field model. Within this physically consistent framework, the motion of the interfaces, the capillary effects, and the complex topological changes experienced by the droplets are simulated in detail. An oil-water emulsion is mimicked: the fluids are considered of same density and viscosity for a range of plausible values of surface tension, resulting in a simplified system that sets a benchmark for further analysis. In the present conditions, the Weber number (We), that is, the ratio between inertia and surface tension, is a primary factor for determining the droplets coalescence rate and the occurrence of breakups. Depending on the value of We, two different regimes are observed: when We is smaller than a threshold value ($We < 1$ in our simulations), coalescence dominates until droplet-droplet interactions are prevented by geometric separation; when We is larger than the threshold value ($We > 1$), a permanent dynamic equilibrium between coalescence and breakup events is established. © *2015 AIP Publishing LLC.* [http://dx.doi.org/10.1063/1.4923424]

I. INTRODUCTION

Turbulent water-oil emulsions are common in the oil production process: the injection of water into the reservoirs to lift the crude oil has the side effect of producing well-mixed water-oil emulsions from which water has to be separated. To increase the separation efficiency, droplet coalescence has to be promoted at large flow rates limiting the undesired droplet fragmentations. These emulsions can be considered as two-phase flows where the dispersed phase can deform, break or coalesce. In the simplest configuration, the fluid system is constituted by two immiscible and incompressible pure components far from their critical point whose interfaces are endowed by surface tension. Although being largely simplified, the physical system is still dominated by complex phenomena characterized by a wide range of scales, from the largest turbulent scale down to the interface thickness. The complete and accurate numerical resolution of all these scales is beyond the current computational limits, as a result only simplified turbulent multiphase systems can be analyzed adopting tailored robust algorithms able to account for the sharp change of physical properties and momentum across the fluid interfaces.

The objective of the work is to investigate the role of the surface tension, here represented by the Weber number (We), in the turbulent dispersion of a swarm of neutrally buoyant droplets; droplets are large compared to the smallest turbulent scale and they can break and coalesce. To

[a]Electronic mail: luca.scarbolo@ge.com. Current address: GE Oil & Gas, Florence 50127, Italy.
[b]Electronic mail: federico.bianco@uniud.it
[c]Electronic mail: soldati@uniud.it. Also at Department of Fluid Mechanics, CISM, Udine 33100, Italy.

the authors knowledge, this work represents one of the first computational efforts towards the study of the collective dynamics of coalescence and breakup of droplets in turbulent wall-bounded flows, setting a benchmark for further analyses and providing a useful numerical framework for the investigation of this class of problems. In the recent past, many authors focused on the theoretical modeling of droplet coalescence and breakup mechanisms,[1,2] showing that coalescence occurs when the drainage of the liquid film between two colliding droplets is faster than the characteristic collision time and proposing a scaling law for the film drainage velocity. Other authors[3] investigated the behavior of deformable droplets and bubbles in turbulent flows focusing on the dispersion of large bubbles in wall-bounded turbulence, limiting the analyses on the wall drag modifications produced by the bubbles and neglecting the simulation of relevant effects such as breakup and coalescence. By contrast, works focused on the coalescence and fragmentation of interfaces in isotropic turbulence[4,5] highlighted the presence of a maximum critical stable droplet diameter, in accordance with theoretical predictions.[6]

The investigation object of this work is performed through a robust and accurate numerical framework specifically tailored for the computational solution of turbulent multiphase flow involving complex topological phenomena. The solution of these class of flows can be ideally considered as a two-steps process: (i) tracking of the fluid-fluid interfaces and (ii) modeling of momentum transfer between the two fluids. To track the surfaces separating different phases, two different techniques can be adopted: Front Tracking (FT) or Front Capturing (FC) methods. FT methods represent the interface as a set of connected points that are advected by the Eulerian flow field.[7,8] FC methods model the interface either as the isosurface of a scalar function (sharp approach) or as a thin volume where the scalar function varies smoothly from different bulk values (continuous approach). Well-known FC methods are Volume-Of-Fluid (VOF),[9,10] Level-Set (LS),[11,12] and the Phase-Field Model (PFM).[13] In order to describe the momentum transfer between the two fluids, the governing equations have to be coupled: steep variation of material properties across the interface has to be numerically resolved and stress interfacial boundary conditions have to be applied. To this purpose, both continuous and sharp techniques can be adopted. In the continuous approach, forces and variations of material properties are smeared over a finite volume region (of few mesh points) across the interface via delta functions; in the sharp approach, the discontinuous nature of the changes are treated as moving boundaries where jump conditions at the interface is preserved without artificially thickening the interfaces. Among the continuous formulations, a widely used technique is the Continuum Surface Force (CSF) method[14] that can be coupled with both FT and FC methods. The sharp approach is represented by the ghost-fluid-method (GFM)[15] which was originally coupled to the LS method and then extended to FT[16,17] and VOF.[18]

The PFM belongs to the continuous methods since it is a FC method coupled with a continuous approximation of surface forces. It has shown promising capabilities in the analysis of the complex coalescence and breakup phenomena[19,20] and for this reason, it has been adopted in this work. Due to its thermodynamic derivation which is rigorous in the case of near critical mixtures (where the interface thickness is non-negligible), interfaces merging or creation are described with no need of additional artificial models. Therefore, this method can be naturally applied to different multiphase problems where phases can be either miscible, immiscible, or partially miscible. It is worth noticing that since the model considers a finite size interface separating different phases, when applying PFM to far-from-critical mixtures, all topological changes that take place at a scale smaller than the interface thickness are filtered out. Nevertheless, its formal convergence to sharp-interface systems has been shown by different authors[13,21,22] and also several rigorous review of the model can be found.[13,23] The PFM has been proven to be able to describe coalescence and drainage regimes in simple shear flows of immiscible fluids,[24] hence it represents a promising method to tackle complex multiphase flows involving coalescence and breakup.

II. PHYSICAL PROBLEM AND MODELING

To study the dynamics of coalescence and breakup of large deformable droplets in wall bounded turbulence, a swarm of $n_{d,0}$ droplets of initial diameter d_0 has been dispersed in a fully

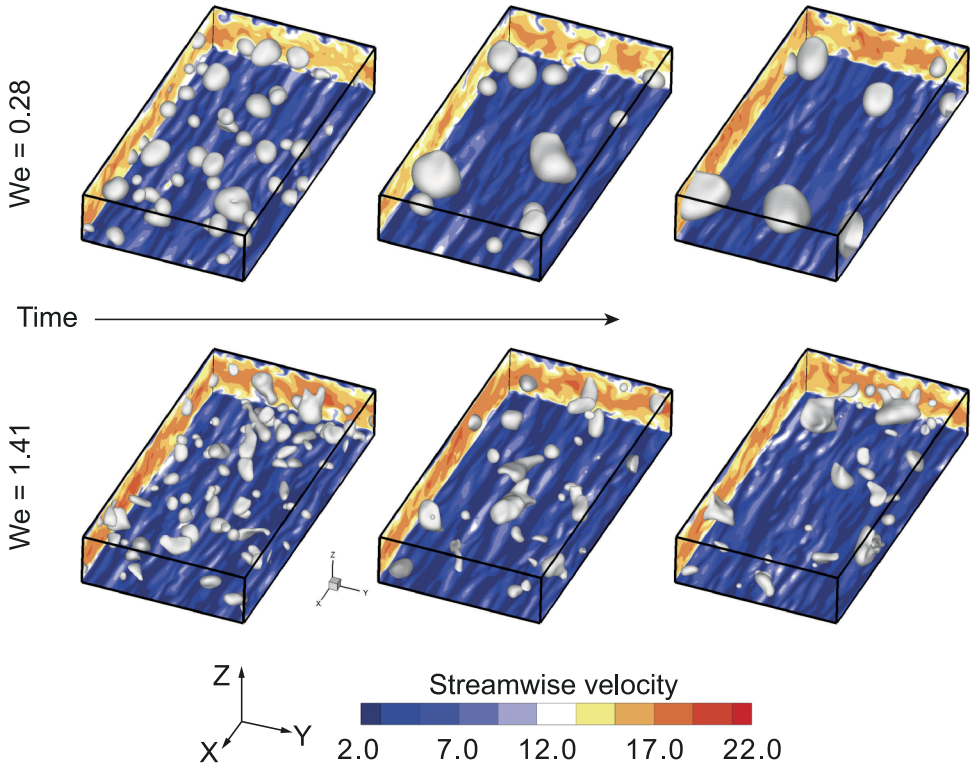

FIG. 1. Droplets evolution in channel flow for two different Weber numbers (upper and lower panel row). Streamwise velocity u is rendered on xy, xz, and yz slices.

developed turbulent channel flow. The two fluids (droplets and the continuous phase) have the same density $\rho_f = \rho_d = \rho$ and the same kinematic viscosity $\nu_f = \nu_d = \nu$ (subscripts f and d stand for continuous phase flow and droplet, respectively) and they are considered immiscible, incompressible, and Newtonian. The fluid interfaces are free from any contaminants (i.e., surfactants or nano-aggregates), as a result droplets coalescence can be prevented only by the film drainage or by the presence of a strong turbulent structure. Under these hypotheses, the resulting physical system is largely simplified, nevertheless the most important features of the problem, the turbulent motion and the droplet-droplet interactions, are conserved and described in great detail. This physical system can be efficiently and accurately described, with reasonable computational resources, adopting a PFM: the present simulations required nearly 2×10^6 cpu-hours on a large scale parallel infrastructure with a raw data production larger than $3TB$. In Fig. 1, two snapshots of the simulated system are reported; the reference frame is located at the center of the channel and x-, y-, and z-axes point in the streamwise, spanwise, and wall-normal directions, respectively. The domain size is $4\pi H \times 2\pi H \times 2H$ in x, y, and z directions, respectively, and H is the channel half-height.

The dimensionless governing equations are the following:

$$\nabla \cdot \mathbf{u} = 0, \tag{1}$$

$$\frac{\partial \mathbf{u}}{\partial t} = -\mathbf{u} \cdot \nabla \mathbf{u} - \nabla p - \nabla \Pi + \frac{1}{Re_\tau} \nabla^2 \mathbf{u} + \frac{3}{\sqrt{8}} \frac{1}{We \cdot Ch} \mu \nabla \phi, \tag{2}$$

$$\frac{\partial \phi}{\partial t} = -\mathbf{u} \cdot \nabla \phi + \frac{1}{Pe} \nabla^2 \mu, \tag{3}$$

$$\mathcal{F}(\phi) = f(\phi) + \frac{1}{2} Ch^2 |\nabla \phi|^2 = \frac{1}{4} (\phi - 1)^2 (\phi + 1)^2 + \frac{1}{2} Ch^2 |\nabla \phi|^2, \tag{4}$$

$$\mu = \frac{\delta \mathcal{F}}{\delta \phi} = \phi^3 - \phi - Ch^2 \nabla^2 \phi. \tag{5}$$

Eqs. (1) and (2) are the incompressible mass and momentum conservation equations, where $\mathbf{u}$ is the incompressible velocity field and p and Π are the fluctuating and mean components of the pressure field, respectively. Eq. (3) is the phase field conservation equation, known as Cahn-Hilliard equation; in the PFM framework, the two components are described as a mixture through a continuous scalar order parameter $\phi(\mathbf{x})$. The order parameter assumes constant values ϕ_+ and ϕ_- in the bulk fluid regions and it is characterized by smooth variations across the fluid-fluid interface. The thermodynamic chemical potential, μ, describes the variation of free energy ($\mathcal{F}(\phi)$) resulting from a small local change of composition of the mixture; the free energy $\mathcal{F}(\phi)$, (4), is the sum of a double-well potential $f(\phi)$ (that keeps in account the phobic behavior) and a non-local term ($Ch^2|\nabla\phi|^2$) that accounts for the non-zero surface tension. Due to surface tension, Eqs. (2) and (3) are coupled via the capillary force term, $\frac{3}{\sqrt{8}}\frac{1}{We\cdot Ch}\mu\nabla\phi$, that describes the momentum exchanged between the two fluids at the interface. Equations (1)-(5) are rewritten in a non-dimensional formulation using the scaling quantities U_τ, H, and ϕ_+, where $U_\tau = \sqrt{\tau_w/\rho}$ is the shear velocity based on the wall shear stress τ_w and the fluid density ρ. The non-dimensional groups that appear in Eqs. (1)-(4) are defined as follows:

$$Re_\tau = \frac{U_\tau H}{\nu}, \qquad Pe = \frac{U_\tau H}{M}, \qquad We = \frac{\rho U_\tau^2 H}{\sigma}, \qquad Ch = \frac{\xi}{H}, \tag{6}$$

where M is the fluid mobility inside the interfacial layer of thickness ξ and surface tension σ. The shear Reynolds number (Re_τ) is the ratio between inertial forces and viscous forces, and the Weber number (We) is the ratio between inertial forces and the surface tension. In the PFM, the Peclet number (Pe) represents the ratio between the diffusive time scale H^2/M and the convective time scale $H/(U_\tau H)$ in the interfacial layer, and it controls the interface characteristic relaxation time; the Cahn number (Ch) is the dimensionless interface thickness (or capillary width).

In this work, Re_τ and We are input parameters that are defined by considering the physical properties of the fluids, the flow regime, and the surface tension; furthermore, the flow is driven by imposing a mean pressure gradient $\nabla\Pi$ along the streamwise direction. Due to the presence of a non-zero capillary force term, the average pressure gradient should be generalized[25] to keep into account the flow driving force and the average capillary forces. Once the shear Reynolds number is fixed, the value of the surface tension is chosen by changing the Weber number. The PFM here adopted is based on a thermodynamic framework that is rigorous when simulating near critical systems, namely, mixtures where the interface thickness is a transition layer of the same order of the problem length scale $Ch \propto O(H)$.[13,23] When considering mixtures of fluids far from critical point, the physical interface thickness is extremely small, of the order of molecular length-scale,[26,27] therefore $Ch \to 0$. The numerical resolution of such interface thickness is beyond the current computational limits (and beyond the continuum hypotheses, as well); thus, for a given spatial discretization, Ch is chosen as the smallest value that guarantees a good (spectral) numerical accuracy.[19] Once the Cahn number is fixed, a consistent "sharp-interface limit"[19,28,29] ($Ch \to 0$) is recovered imposing $Pe \propto Ch^{-1}$. As shown by means of formal asymptotic expansions,[22] in such limit, Cahn-Hilliard equation (3) describes the advection of the order parameter ϕ, preventing the degradation of the interface profile. As a result, the value of surface tension σ is correctly represented and the capillary force coupling term in the Navier-Stokes equations (1) and (2) is equivalent to any CSF formulation.[14]

A. Modeling of capillary effects

In the PFM framework, surface tension forces are transformed to volume forces acting in a small finite region, via delta functions; in order to highlight the common features of PFM with other CSF models, the capillary force $\mathbf{f}_c$ of the momentum equations (2) is exploited,

$$\mathbf{f}_c = \frac{3}{\sqrt{8}}\frac{1}{ChWe}\left(\mu\nabla\phi - \nabla f\right) = -\frac{3}{\sqrt{8}}\frac{1}{ChWe}\left[Ch^2\left(\nabla\cdot\nabla\phi\right)\nabla\phi\right], \tag{7}$$

where the pressure gradient in Eq. (2) has been split:[13,21] $\nabla p = \nabla\tilde{p} + \nabla f = \nabla\tilde{p} + (\phi^3 - \phi)\nabla\phi$.

Starting from a scalar field ϕ, the average curvature $\kappa = (\kappa_1 + \kappa_2)/2$ and the local normal vector $\mathbf{n}$ of each level-set curve are

$$\kappa = -\nabla \cdot \left(\frac{\nabla \phi}{|\nabla \phi|} \right) = -\frac{\nabla^2 \phi}{|\nabla \phi|} + \frac{1}{|\nabla \phi|^2} \nabla \phi \cdot \nabla \left(|\nabla \phi| \right), \tag{8}$$

$$\mathbf{n} = -\frac{\nabla \phi}{|\nabla \phi|}, \tag{9}$$

where definitions (8) and (9) are valid only if ϕ has the properties of a signed function, namely, if each of its iso-surfaces is parallel to the others. This property is conserved when advecting ϕ through Cahn-Hilliard equation (3), adopting the $Pe \propto Ch^{-1}$ scaling.[22] In this way, the controlled diffusion within the interfacial layer is fast enough to restore the local modification of the interface profile produced by the convective effects. As a result, the profile of ϕ across the interface, along the interface-normal coordinate s, is always $\phi(s) = \tanh[s/(\sqrt{2}Ch)]$ which has the properties of a signed function. Substituting (8) and (9) into Equation (7), the capillary force yields

$$\mathbf{f}_c = -\frac{3}{\sqrt{8}} Ch |\nabla \phi|^2 \cdot \frac{\kappa}{We} \mathbf{n} + \frac{3Ch}{\sqrt{8}We} \nabla \phi \cdot \nabla \left(|\nabla \phi| \right) \mathbf{n}. \tag{10}$$

The following δ-function can be isolated:

$$\frac{3}{\sqrt{8}} |\nabla \phi|^2 Ch = \delta(\mathbf{x}) \Longrightarrow \int_s \delta(\mathbf{x}) \mathrm{d}s = 1, \tag{11}$$

where the integral is performed along an interface-normal direction s and the integration extrema are, by definition, $\pm\infty$. Integrating in the same way Equation (10), the equivalent surface force applied on a sharp interface is obtained,

$$\int_s \mathbf{f}_c \mathrm{d}s = -\frac{\mathbf{n}}{We} \int_s \delta(\mathbf{x}) \kappa \mathrm{d}s + \int_s \left(\frac{3Ch}{\sqrt{8}We} \nabla \phi \cdot \nabla \left(|\nabla \phi| \right) \mathbf{n} \right) \mathrm{d}s \simeq \frac{\kappa_0}{We} \mathbf{n}, \tag{12}$$

where the second integral on the RHS vanishes (integral of the product between a symmetric positive function and an antisymmetric function). The difference between $\int \delta\kappa$ and κ_0 is due to the computation of the local curvature that is based on a finite thickness layer rather than on a zero-thickness layer. The error committed with this approach is in any case small when the curvature radius is large with respect to the interface thickness. The same conclusions of the derivation above have been obtained either through a similar approach[21] or adopting a variational approach.[13] The result reported here can be generalized to physical systems with non-uniform surface tension: in that case, the Marangoni force[30] term is recovered by introducing a non-constant Cahn number.[31,32]

B. Simulation parameters

The equations system (1)-(5) has been solved using a pseudo-spectral approach[33,34] where periodic boundary conditions have been applied along the homogeneous streamwise and spanwise directions (x and y) for both velocity field and order parameter. The wall boundary conditions for velocity are the usual no-slip conditions. For the interface advection, we impose a normal contact angle condition.[19,35] In this way, droplets are free to interact with the walls by creating contact lines. An initial number of $n_{d,0} = 256$ droplets of diameter $d = 0.6$ have been initialized superposing the scalar field ϕ over a fully developed turbulent flow obtained from previous single phase simulations. Since the two fluids are density and viscosity matched, the initial transient is extremely fast. The volume fraction of the droplets id $\varphi = 0.054$ and the simulations have been performed considering a wide range of Weber numbers: $We = 0.18 \div 2.8$.

In order to consider a fully developed turbulent flow, the shear Reynolds number is set $Re_\tau = 150$; in this regime, the initial droplet diameter is much larger than the Kolmogorov length scale η_κ and the ratio between the Kolmogorov length scale and the droplet diameter is $0.027 \leq \eta_\kappa/d_0 \leq 0.063$. Simulations were run on a $512 \times 256 \times 257$ fixed cartesian grid fine enough to resolve the smallest length scale of the turbulent flow, while the time step $\Delta t = 10^{-4}$ has been chosen to resolve the smallest temporal scales and respond to the numerical stability requirements associated with the grid resolution. The pseudo-spectral scheme adopted can resolve accurately the interfacial layer with a

minimum number of three mesh-points.[19,36] Here, the interface is described by three mesh-points along x and y directions (where a uniform discretization is adopted) and by a minimum number of seven mesh-points along the z direction where a finer non-uniform discretization is adopted (Chebyshev polynomials). With the grid resolution adopted, the interface thickness (a layer where $-0.9 \leq \phi \leq 0.9$) is fixed choosing $Ch = 0.0185$ and, according to the scaling law,[22] the Peclet number is $Pe = 162.2$. These parameters ensure that the PFM converges to the "sharp interface limit." In addition, we can also grant that the pseudo-spectral algorithm can solve correctly Eq. (2) for local capillary forces (12) for the chosen range of the Weber number. The interface thickness is larger than the Kolmogorov length scale $0.36 \leq \eta_\kappa/Ch \leq 0.84$, thus the interface cannot be deformed by eddies of that size. This drawback is unavoidable when smearing the interfacial forces over a finite thickness layer, thus it afflicts all the CSF methods; however, the size of the damped eddies is in any case small compared to the droplet diameter. The PFM cannot completely fulfill local mass conservation.[20,36] However, due to the accuracy of the numerical method and to the small interface thickness adopted, the mass loss is in any case small: specifically, after the entire simulation (2.5×10^5 time-steps and $4000t^+$, corresponding to ~50 channel length covered by the mean flow), the mass loss ranges from 2% for the smallest *We* to 10% for the largest *We*.

III. RESULTS AND DISCUSSION

The scalar field ϕ is initialized so that different sets of droplets with the same Weber number are released in a fully developed turbulent flow in an equally spaced arrangement whose center of mass is set at distance $z = 54w.u.$ from the wall. Droplets are superposed to an initial velocity field obtained from previous fully developed single phase simulations; the time needed for the flow to adapt to the superposition of the scalar field ϕ is extremely short.[36] This is because only the capillary forces at the droplets interfaces need to be balanced, and the choice of *Pe* ensures an interface relaxation time much faster than the time scale of the external convective forcing. As a result, relaxation of the initial interface profile is almost instantaneous. Upon injection, droplets are advected by the flow and undergo two distinct phenomena: segregation towards the center of the channel and droplet-droplet interaction. Due to segregation, droplets tend to concentrate in the center of the channel, with the consequent negligible probability of collision with the walls, which in the entire simulation was never observed. In this work, we focus our analyses to the droplet-droplet interactions, only. In Figs. 2 and 3, examples of coalescence and breakup dynamics as they appear in our simulations are depicted. We could not find previous experimental investigations referring to systems with two fluids of the same density, yet the qualitative behavior of such events does not appear in contrast with the experimental observations[37,38] despite the large density ratio considered in those works. These events strongly depend on the *We* number and take place multiple times in different places of the domain. The snapshots of Fig. 3 show a typical time evolution of a breakup event: a droplet deformed by local velocity fluctuations and shear is stretched until a thin bridge of fluid is formed; the thin bridge is then broken by surface tension forces that tend to minimize the energy stored in the interface. As an opposite case, the snapshots of Fig. 2 depict a time evolution of

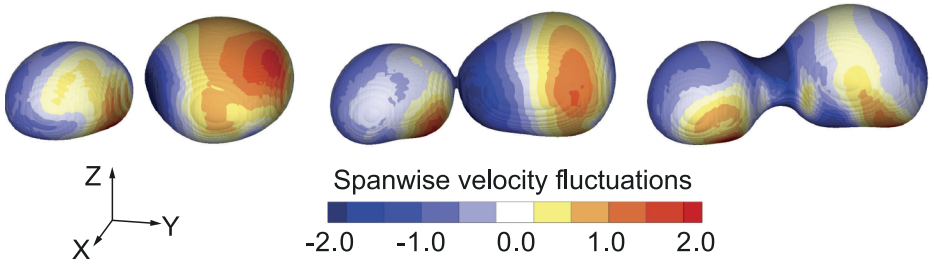

FIG. 2. Time evolution of the coalescence process depicted in the top panels of Fig. 5. The snapshots are taken at time distances of $15t^+$ and the spanwise velocity fluctuations v'^+ are rendered over the droplets isosurfaces (that are identified by $\phi = 0$).

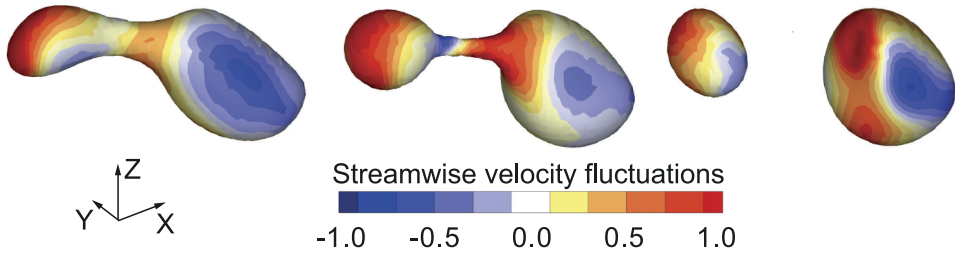

FIG. 3. Time evolution of a breakup event observed in the $We = 1.41$. The snapshots are taken at time distances of $15t^+$ starting from an initial time of $1170t^+$. The streamwise velocity fluctuations u'^+ are rendered over the droplets isosurfaces.

a typical coalescence event: droplets are forced to collide by the external flow field; in the collision region a bridge forms, then the surface tension starts to restore the sphere-like shape of the droplet (which minimizes the energy stored in the interface). Within the PFM framework, these dynamics are captured without the adoption of any artificial model, thus this method is a good candidate to investigate, with the limitations explained in Sec. II, the collective dynamics of coalescence and breakup.

A. Dynamics of the dispersed phase

The droplets are allowed to interact and collide under the action of the turbulent flow field: their dynamics is controlled both by the mean shear and the turbulent fluctuations.

Let us consider two colliding droplets. In general, not every collision results in a coalescence event and, in particular, two leading mechanisms can prevent the coalescence: (i) turbulent fluctuations that cause a trajectory deviation so that droplets move away from each other preventing collision and (ii) the presence of a thin film between the colliding droplets, which does not drain rapidly enough causing the bouncing.

Supported by the simple scaling analyses reported below, the first mechanism appears to be more efficient and, as a result, coalescence is expected to be the most likely event when the two droplets collide. In particular, approximating two droplets as spheres of diameter $d_l > d_s$ with $d_l \sim O(d_s)$ colliding at velocity u_r, their collisional momentum Q_d can be estimated. In a similar way, the momentum of the thin film of fluid that separates two colliding droplets Q_f can be estimated,

$$Q_d = \rho_f \frac{4\pi d_s^3}{3} u_r, \qquad Q_f = \rho_f h_f \frac{\pi \ell_f^2}{4} u_f. \tag{13}$$

The film is approximated by a thin disk of height h_f and diameter ℓ_f while u_f is the characteristic velocity at which the film is drained; u_f can be estimated adopting the lubrication theory into the film:[2] $u_f \simeq (2\sigma h_f^2)(\mu_f d_s \ell_f)$. Hence, the film-droplet inertial ratio results,

$$\frac{Q_f}{Q_d} \sim \left(\frac{\rho_f}{\rho_d}\right)\left(\frac{d_s}{\ell_f}\right)\left(\frac{u_\tau}{u_r}\right)\left(\frac{Re_\tau}{We}\right)\left(\frac{h_f}{d_s}\right)^3. \tag{14}$$

In our simulations, $\rho_f/\rho_d = 1$ and the ratio d_s/ℓ_f can be safely considered as $O(1)$. Estimating u_r as the time-averaged relative velocity between the droplet pairs characterized by the minimum droplet pair distance, the ratio $\langle u_\tau/u_r \rangle$ is of $O(1)$ for every set of tested Weber number. We explore regimes Re_τ/We from $O(10^2)$ to $O(10^3)$, while $(h_f/d_s)^3$ varies in time, at least in the initial transient, because droplets increase in volume while they coalesce. However, since h_f is of the order of the interface thickness ($h_f \simeq 4Ch \simeq 0.04$), on average $O(2 \times 10^{-6}) \leq \langle (h_f/d_s)^3 \rangle \leq O(10^{-4})$. Consequently, the ratio Q_f/Q_d varies from $O(10^{-1})$ to $O(10^{-4})$ meaning that, in average, colliding droplets have larger inertia with respect to the thin fluid film. The local Reynolds number into the film can be roughly estimated as

$$Re_f = \frac{\rho_f u_f h_f}{\mu_f} = \frac{Re_\tau^2}{We} \frac{h_f^3}{d_s^2 H}. \tag{15}$$

Re_f is relatively small at the early stages of the simulations ($O(10^{-2})$ for large *We*) because of the small droplets diameters but, in general, it becomes large once the droplets grow (up to $O(10^1)$ for the largest droplets and the smallest *We*). Therefore, since droplet inertia is larger with respect to film inertia and viscous forces into the film play a minor role during drainage, droplets bouncing is likely to be observed only in the early stages of simulations while, most of the time, the coalescence of two colliding droplets is expected. Hence, the only way to prevent coalescence, when droplets are large, is avoiding collision by transport mechanisms. It is worth to observe that, due to the so called reflexive separation mechanism,[37,38] a coalescence event occurring after a collision could still result in a subsequent breakup. Due to the wall-bounded turbulence and the zero density contrast between the phases, the droplets relative velocity is in general small. This corresponds to the relative Weber number[37,38] $We_r = We(u_r/u_\tau)(d_s/H)$ being of $O(1)$ making the reflexive separation unlikely to be observed in this work.

The number of distinct droplets in the channel ($n_d/n_{d,0}$) is shown in Fig. 4(a) as function of time for different Weber numbers. As expected, $n_d/n_{d,0}$ decreases in time and it stabilizes toward an asymptotic value after a long transient. Consequently the average droplet diameter $\langle d \rangle$ increases in time due to the coalescence events and volume conservation (Fig. 4(b)). Two different dynamics of coalescence are observed depending on the Weber number.

1. Small Weber number: We < 1

For small Weber numbers, a continuous reduction of the number of droplets ($n_d/n_{d,0}$) is observed. This trend is possible only if coalescence events dominate over the breakups events; however, from a detailed analyses of the droplet fields, breakup appears to be remote events. This behavior is consistent with the relative importance of inertial forces with respect to surface tension at small Weber numbers ($We < 1$). To shed some light on the coalescing events, in Fig. 5, the time evolution of a coalescence event (top panels) is compared with the case in which the collision is prevented (bottom panels). The fluctuating streamwise velocity field is rendered on a slice crossing the two droplets. Coalescence or separation of the droplets is driven by the successive flow regions experienced by the droplets. In the bottom panels, at the beginning, both droplets are experiencing a similar velocity region, as a result their distance is not reduced. After $15t^+$, the front droplet encounters a region of positive velocity fluctuations that drives it apart from the droplet behind. After $30t^+$, the droplets are separated by different spanwise velocities, indicating that the large scales turbulent structures encountered are, in this case, preventing the coalescence. It is worth noticing that in case of no coalescence, the liquid film between the droplets produces only a slightly flattening of the front droplet interface and, proceeding in time, the local shape do not differ much from a spherical shape ($\ell_f < d_s$). In this case, as predicted in the momentum scaling of Sec. III, the film inertia is negligible and the collision dynamics is controlled by the velocity field. On the contrary, the

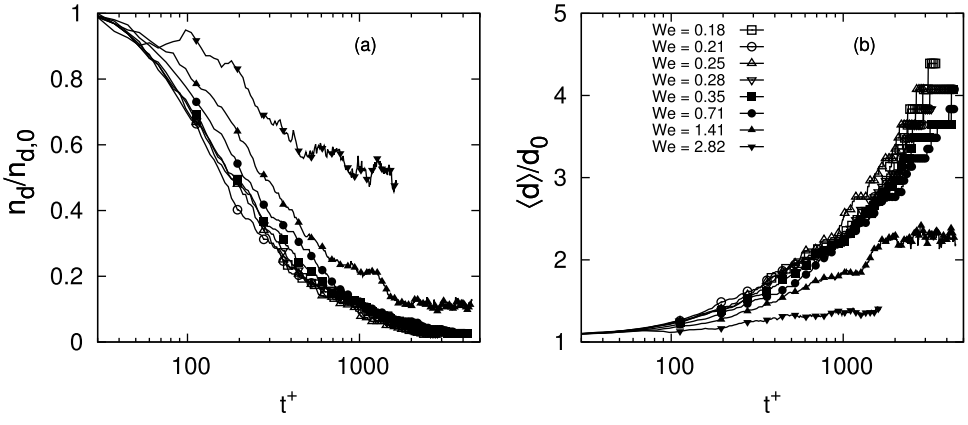

FIG. 4. Time evolution of the normalized number of droplets $n_d/n_{d,0}$ (panel (a)) and normalized mean diameter $\langle d \rangle/d_0$ (panel (b)) as function of the Weber number *We*.

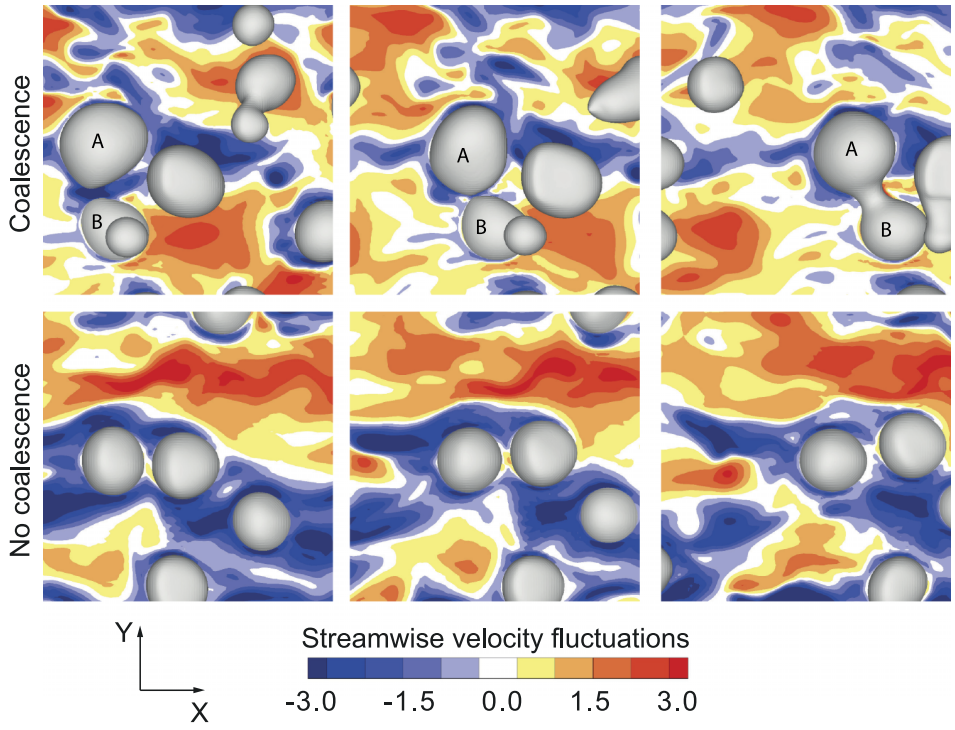

FIG. 5. Time evolution of two coalescing droplets (top panels) and two non-coalescing droplets (bottom panels) taken at time distances of $15t^+$. The streamwise velocity fluctuations u'^+ are rendered over a $x-y$ plane crossing the droplets ($z^+ = 50w.u.$ and $z^+ = 250w.u.$ for the top panels and bottom panels, respectively). The time sequences are taken at the same initial time $390t^+$, at different positions on the computational domain and for $We = 0.18$.

initially non-homogeneous flow regions encountered by the coalescing droplets (A and B depicted in the top panels) move the droplets closer fostering collision. The fluid film is squeezed by the motion of the droplets and, as a result, large negative streamwise velocity fluctuations ($u'^+ \simeq 3$) can be observed into the film. After $15t^+$, the film is completely drained and the droplets interface collide; after $30t^+$, a large bridge between the droplets is generated. It is worth to notice that the coalescence can take place because the film drainage characteristic time ℓ_f/u_f is smaller than the characteristic collision time[1] h_f/u_r. In fact, in this case, $u_f \simeq 3\langle u_r \rangle$, and $h_f \simeq \ell_f$, since no flattening of the droplet is observed. Fig. 2 helps to clarify the coalescence driving mechanism: it is evident that the spanwise velocity fluctuations are acting to push the droplets tips close together. Combining top panel of Figs. 5 and 2, a coalescing event in a xy plane can be summarized: (i) the spanwise velocity fluctuations push the droplets closer, (ii) the film drains in the streamwise direction helped by the local velocity fluctuations, and (iii) the bridge between the droplets forms.

Finally, in the early stages ($t^+ < 2000$), the coalescing regime shows a weak dependence from We, while, for $t^+ > 2000$ the number of droplets observed in the asymptotic regime is almost universal (Fig. 4(a)). As shown in Fig. 4(b), the droplet coalescence produces an increment of the droplet average diameter $\langle d \rangle$. In the first stages of the simulation, $\langle d \rangle < H$ and the droplets are subjected to a turbulent mixing that promotes their interactions. Due to the increments in size, the droplet motion decorrelates from turbulent scales of size smaller than $\langle d \rangle$ that can only deform the interface. When $t^+ > 1000$, $\langle d \rangle > H$ and the droplets motion starts to be controlled by the average velocity field, rather than by the turbulent fluctuations. Fig. 6(a) shows the minimal distance between the two closest droplets, averaged over all the droplets pair $\langle l_m \rangle$ and normalized by the average droplet diameter $\langle d \rangle$. In the case of small Weber numbers, the distance increases in time, consequently the probability of interaction decreases in time. At large times, the minimal distance can be $\langle l_m \rangle / \langle d \rangle \simeq 2 \div 3$, such that droplets are essentially too distant to interact and coalescences are dramatically reduced. In particular, the ratio $\langle l_m \rangle / \langle d \rangle$ at which the droplet-droplet interactions cease is smaller than that observed for point-wise particles in turbulence.[39] This behavior is likely

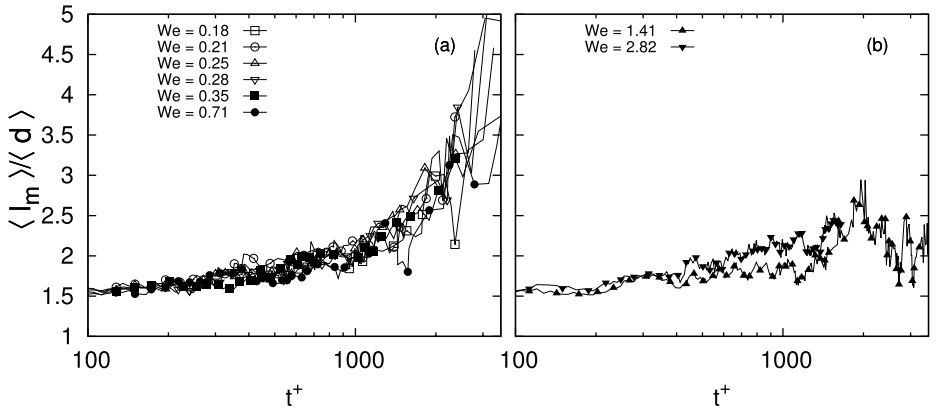

FIG. 6. Time evolution of the average minimal distance $\langle l_m \rangle$ normalized by the average droplet diameter $\langle d \rangle$. Small Weber numbers ($We < 1$) are reported in panel (a). Large Weber numbers ($We > 1$) are reported in panel (b) where the case $We = 0.71$ is also shown for sake of comparison.

due to the droplets size that is large enough to make them insensitive to a significant portion of the turbulence spectrum.

2. Large Weber number: We > 1

In the case of large *We*, as for small *We* but with a shorter transient, $n_d/n_{d,0}$ decreases in time until an asymptotic behavior is reached. However, if *We* is larger than a critical value ($We > 1$, in this work), the reduction of n_d is not strictly monotonic. Such behavior is due to the alternate imbalance between coalescence and the breakups produced by the combined action of mean and turbulent shear stress. As shown in Fig. 4, local increments of the number of droplets are observed after an early transient in which breakups are rare. Indeed, at this stage ($t^+ < 1000$), droplets are small and the local turbulent shear can produce very large deformations only if *We* is very large. As a result $n_d/n_{d,0}$ is first dominated by coalescence. Growing in size, droplets can be large enough to be subjected to velocity fluctuations that break them. This behavior is consistent with the theory of the critical stable diameter[6] and the recent numerical results for homogeneous and isotropic turbulence.[4,5] After the initial transient, an asymptotic regime (in the statistical sense) is reached and coalescence/breakup events are in a dynamic equilibrium. Droplets generated by breakup are compensated by other coalescences and, as a result, at equilibrium the number of droplets is much larger than that observed in the case of small Weber numbers. For instance, $We = 1.41 \div 2.82$ leads to a steady number of droplets that is from one to two magnitude orders larger than the small Weber number cases, Sec. III A 1. Fig. 3 depicts the time evolution of a droplet breakup: (i) subjected to the local velocity field, the droplet loses its initial sphere-like shape; (ii) the droplet deforms assuming an elongate shape with a neck; and (iii) finally, the pinch-off take place. Observing the streamwise velocity fluctuations u'^+ rendered over the droplet surface, it can be shown that the local velocity field is responsible to create a curvature that will allow the surface tension to complete the breakup. When the concave curvature is produced, the local velocity field tends to pull apart the thin neck helping surface tension to finalize the breakup. Fig. 6(b) shows how the breakup introduces an upper bound to $\langle l_m \rangle/\langle d \rangle$ which, on average, for this regimes is smaller than $3\langle d \rangle$. Due to this bound, the probability of droplet-droplet collisions and coalescences is large, and droplets easily coalesce and grow to a diameter beyond the critical size (for a given *We*) resulting in a new breakup. This is essentially the mechanism that leads to the permanent dynamical equilibrium observed in Fig. 4(a).

IV. CONCLUSIONS

The coalescence and breakup of swarm of large breaking and coalescing droplets dispersed in a fully turbulent channel flow has been investigated with a phase field model. This method does not require any fictitious treatment of coalescence and breakup events: its thermodynamics origin

allows to accurately describe the interfacial topological changes, furthermore it can be efficiently implemented in a pseudo-spectral numerical framework. It has been shown that two different droplet-droplet interaction regimes can be observed depending on the Weber number (*We*, that is, the ratio between inertia and surface tension). For small Weber ($We < 1$), coalescence dominates: in such regime, surface tension prevents fragmentation and a continuous decrement of the normalized number of droplets $n_d/n_{d,0}$ is observed until a universal asymptotic regime is reached. At large t^+, coalescence becomes a rare event because droplets are too distant to interact and $n_d/n_{d,0}$ stabilizes to a value that is *We* independent. On the contrary, for large Weber numbers ($We > 1$), $n_d/n_{d,0}$ does not decrease continuously. Local turbulence can cause droplets fragmentation if the diameter of a droplet is larger than a critical value and a dynamic equilibrium between coalescence and break-up is reached at large t^+. The asymptotic number of droplets is function of *We* and it can be one to two order of magnitude larger than the number of droplets observed for $We < 1$.

ACKNOWLEDGMENTS

The authors acknowledge the CINECA for the availability of high performance computing resources and support. The research was supported by the Italian Ministry for Research under the 2009 PRIN program "Phase-field approach to chaotic mixing."

[1] H. Yang, C. C. Park, Y. T. Hu, and L. G. Leal, "The coalescence of two equal-sized drops in a two-dimensional linear flow," Phys. Fluids **13**, 1087–1106 (2001).
[2] J. Frostad, J. Walter, and L. Leal, "A scaling relation for the capillary-pressure driven drainage of thin films," Phys. Fluids **25**, 052108 (2013).
[3] J. Lu and G. Tryggvason, "Effect of bubble deformability in turbulent bubbly upflow in a vertical channel," Phys. Fluids **20**, 040701 (2008).
[4] S. Berti, G. Boffetta, M. Cencini, and A. Vulpiani, "Turbulence and coarsening in active and passive binary mixtures," Phys. Rev. Lett. **95**, 224501 (2005).
[5] P. Perlekar, L. Biferale, M. Sbragaglia, S. Srivastava, and F. Toschi, "Droplet size distribution in homogeneous isotropic turbulence," Phys. Fluids **24**, 065101 (2012).
[6] J. O. Hinze, "Fundamentals of the hydrodynamic mechanism of splitting in dispersion processes," AIChE J. **1**, 289–295 (1955).
[7] S. O. Unverdi and G. Tryggvason, "A front-tracking method for viscous, incompressible, multi-fluid flows," J. Comput. Phys. **100**, 25–37 (1992).
[8] G. Tryggvason, B. Bunner, A. Esmaeeli, D. Juric, N. Al-Rawahi, W. Tauber, J. Han, S. Nas, and Y.-J. Jan, "A front-tracking method for the computations of multiphase flow," J. Comput. Phys. **169**, 708–759 (2001).
[9] C. W. Hirt and B. D. Nichols, "Volume of fluid (vof) method for the dynamics of free boundaries," J. Comput. Phys. **39**, 201–225 (1981).
[10] D. Gueyffier, J. Li, A. Nadim, R. Scardovelli, and S. Zaleski, "Volume-of-fluid interface tracking with smoothed surface stress methods for three-dimensional flows," J. Comput. Phys. **152**, 423–456 (1999).
[11] S. Osher and J. A. Sethian, "Fronts propagating with curvature-dependent speed: Algorithms based on hamilton-jacobi formulations," J. Comput. Phys. **79**, 12–49 (1988).
[12] S. Osher and R. P. Fedkiw, "Level set methods: An overview and some recent results," J. Comput. Phys. **169**, 463–502 (2001).
[13] D. M. Anderson, G. B. McFadden, and A. A. Wheeler, "Diffuse-interface methods in fluid mechanics," Annu. Rev. Fluid Mech. **30**, 139–165 (1998).
[14] J. Brackbill, D. B. Kothe, and C. Zemach, "A continuum method for modeling surface tension," J. Comput. Phys. **100**, 335–354 (1992).
[15] R. P. Fedkiw, T. Aslam, B. Merriman, and S. Osher, "A non-oscillatory Eulerian approach to interfaces in multimaterial flows (the ghost fluid method)," J. Comput. Phys. **152**, 457–492 (1999).
[16] H. Terashima and G. Tryggvason, "A front-tracking/ghost-fluid method for fluid interfaces in compressible flows," J. Comput. Phys. **228**, 4012–4037 (2009).
[17] Y. Hao and A. Prosperetti, "A numerical method for three-dimensional gas–liquid flow computations," J. Comput. Phys. **196**, 126–144 (2004).
[18] T. Ménard, S. Tanguy, and A. Berlemont, "Coupling level set/vof/ghost fluid methods: Validation and application to 3d simulation of the primary break-up of a liquid jet," Int. J. Multiphase Flow **33**, 510–524 (2007).
[19] V. E. Badalassi, H. D. Ceniceros, and S. Banerjee, "Computation of multiphase systems with phase field models," J. Comput. Phys. **190**, 371–397 (2003).
[20] P. Yue, C. Zhou, and J. J. Feng, "Spontaneous shrinkage of drops and mass conservation in phase-field simulations," J. Comput. Phys. **223**, 1–9 (2007).
[21] R. Chella and J. Viñals, "Mixing of a two-phase fluid by cavity flow," Phys. Rev. E **53**, 3832 (1996).
[22] F. Magaletti, F. Picano, M. Chinappi, L. Marino, and C. M. Casciola, "The sharp-interface limit of the cahn-hilliard/navierstokes model for binary fluids," J. Fluid Mech. **714**, 95–126 (2013).
[23] A. G. Lamorgese, D. Molin, and R. Mauri, "Phase field approach to multiphase flow modeling," Milan J. Math. **79**, 597–642 (2011).

[24] O. Shardt, J. J. Derksen, and S. K. Mitra, "Simulations of droplet coalescence in simple shear flow," Langmuir **29**, 6201–6212 (2013).
[25] A. Lamorgese and R. Mauri, "Diffuse-interface modeling of phase segregation in liquid mixtures," Int. J. Multiphase Flow **34**, 987–995 (2008).
[26] D. M. Mitrinović, A. M. Tikhonov, M. Li, Z. Huang, and M. L. Schlossman, "Noncapillary-wave structure at the water-alkane interface," Phys. Rev. Lett. **85**, 582 (2000).
[27] A. Giacomello, S. Meloni, M. Chinappi, and C. M. Casciola, "Cassie–baxter and wenzel states on a nanostructured surface: Phase diagram, metastabilities, and transition mechanism by atomistic free energy calculations," Langmuir **28**, 10764–10772 (2012).
[28] V. Kendon, "Scaling theory of three-dimensional spinodal turbulence," Phys. Rev. E **61**, R6071 (2000).
[29] V. M. Kendon, M. E. Cates, I. Pagonabarraga, J.-C. Desplat, and P. Bladon, "Inertial effects in three-dimensional spinodal decomposition of a symmetric binary fluid mixture: A lattice Boltzmann study," J. Fluid Mech. **440**, 147–203 (2001).
[30] L. G. Leal, *Advanced Transport Phenomena: Fluid Mechanics and Convective Transport Processes* (Cambridge University Press, 2007).
[31] D. Jacqmin, "Contact-line dynamics of a diffuse fluid interface," J. Fluid Mech. **402**, 57–88 (2000).
[32] A. Lamorgese and R. Mauri, "Liquid mixture convection during phase separation in a temperature gradient," Phys. Fluids **23**, 034102 (2011).
[33] L. Scarbolo and A. Soldati, "Turbulence modulation across the interface of a large deformable drop," J. Turbul. **14**, 27–43 (2013).
[34] L. Scarbolo and A. Soldati, "Wall drag modification by large deformable droplets in turbulent channel flow," Comput. Fluids **113**, 87–92 (2014).
[35] P. Yue, J. J. Feng, C. Liu, and J. Shen, "A diffuse-interface method for simulating two-phase flows of complex fluids," J. Fluid Mech. **515**, 293–317 (2004).
[36] L. Scarbolo, D. Molin, P. Perlekar, M. Sbragaglia, A. Soldati, and F. Toschi, "Unified framework for a side-by-side comparison of different multicomponent algorithms: Lattice Boltzmann vs. phase field model," J. Comput. Phys. **234**, 263–279 (2013).
[37] N. Ashgriz and J. Poo, "Coalescence and separation in binary collisions of liquid drops," J. Fluid Mech. **221**, 183–204 (1990).
[38] J. Qian and C. Law, "Regimes of coalescence and separation in droplet collision," J. Fluid Mech. **331**, 59–80 (1997).
[39] C. T. Crowe, J. D. Schwarzkopf, M. Sommerfeld, and Y. Tsuji, *Multiphase Flows with Droplets and Particles* (CRC Press, 2011).